International Journal of Hydrogen Energy 129 (2025) 199–210

Contents lists available at ScienceDirect

International Journal of Hydrogen Energy

journal homepage: www.elsevier.com/locate/he

First-principles calculations on the physical properties of Zr-based perovskites $LiZrH_3$ and $KZrH_3$ for potential hydrogen storage applications

A. Candan [a,*], S. Akbudak [b]

[a] Department of Machinery and Metal Technology, Kırşehir Ahi Evran University, 40100, Kırşehir, Turkey
[b] Vocational School of Health Services, Adiyaman University, 02040, Adiyaman, Turkey

ARTICLE INFO

Handling Editor: Dr M Mahdi Najafpour

Keywords:
Hydrogen storage
Zr-based hydrides
Mechanical properties
Electronic properties

ABSTRACT

Hydrogen is a promising alternative to fossil fuels due to its abundance on Earth, clean-burning properties, and non-toxic nature. However, developing efficient storage solutions remains a major challenge. Perovskite-type hydrides have attracted significant interest as potential solid-state hydrogen storage materials, owing to their high storage density and safety advantages. In this study, Density Functional Theory is employed to conduct a comprehensive investigation of the structural, dynamic, mechanical, and optoelectronic properties of $XZrH_3$ (X = Li and K) to assess their suitability for hydrogen storage. Electronic structure analysis reveals that both materials exhibit metallic behavior. Mechanical properties such as bulk modulus (B), shear modulus (G), Cauchy pressure (C_P), B/G ratio, and Young's modulus (E) are calculated using the Voigt-Reuss-Hill approach. The results indicate that $LiZrH_3$ exhibits ductile behavior, while $KZrH_3$ is characterized as brittle. Both compounds are thermodynamically and mechanically stable, as confirmed by their negative formation enthalpies and elastic constants. Furthermore, the calculated gravimetric hydrogen storage capacities of $LiZrH_3$ and $KZrH_3$ are 2.99 wt % and 2.27 wt%, respectively, with estimated hydrogen desorption temperatures of 473.76 K and 421.06 K. These findings support the potential of Zr-based perovskite hydrides for next-generation hydrogen storage technologies.

1. Introduction

Energy forms the basis of the high standard of living achieved by developed countries today. This situation indicates that the consumption of natural resources will persistently increase to sustain the current level of development and support the progress of developing countries. Fossil resources like oil, natural gas, and coal today meet a large portion of energy needs. However, their limited reserves and environmental damage doom these resources to depletion. In this context, the development of environmentally friendly, renewable, and sustainable energy sources is of enormous importance. Comprehensive studies conducted in the literature reveal that interest in sustainable hydrogen storage materials has significantly increased recently due to the rising energy crisis and environmental issues [1–4]. As a clean energy carrier, hydrogen stands out, and there is a need for safe and highly efficient storage technologies for its effective integration into energy systems.

In hydrogen storage, there are various techniques, such as solid-state hydrogen storage, the liquefaction method, and compressed gas [5–7]. Hydrogen in the gas phase is stored in the form of compressed gas within high-pressure tanks. This method requires the use of vessels that are resistant to high pressure, lightweight, durable, and highly resistant to explosions. However, the low volumetric storage density in compressed hydrogen gas systems constitutes a significant disadvantage. On the other hand, hydrogen in its liquid form is stored using the liquefaction method. In this method, although the density of volumetric storage increases, the system must be maintained at temperatures below 20 K for hydrogen to remain in liquid form. In this context, there are still significant challenges in systems for storing compressed and liquid hydrogen in vehicle technologies.

To overcome these challenges, researchers are developing alternative technologies based on nanostructured materials and metal hydrides that allow for the storage of hydrogen in the solid phase [8–10]. Solid-state hydrogen storage is a unique method for long-term storage. Solid-state hydrogen storage technologies allow the storage of hydrogen using various materials, such as complex hydrides, chemical hydrides, magnesium-based alloys, and intermetallic compounds [6,8,11]. These technologies have high storage capacities and can be evaluated in industrial applications. Currently, the most widely accepted hydrogen

* Corresponding author.
E-mail addresses: cndn14@gmail.com, acandan@ahievran.edu.tr (A. Candan).

https://doi.org/10.1016/j.ijhydene.2025.04.189
Received 6 February 2025; Received in revised form 8 April 2025; Accepted 10 April 2025
Available online 24 April 2025

storage method is the use of hydrogen in the form of compressed gas [12]. However, this method's limited storage capacity and the potential danger it poses without adequate precautions are among its significant disadvantages [13]. Additionally, storing hydrogen in underground natural tunnels is also possible, and this method offers a cost-effective option. Therefore, the development of new hydrogen storage technologies is of major importance for the widespread adoption of renewable and clean energy sources [14,15].

Perovskite hydrides have garnered significant interest as promising candidates for solid-state hydrogen storage due to their high gravimetric hydrogen storage densities. These densities can reach values between 5 % and 8 % [16]. Compounds such as MgH_2 and LiH are among the hydride examples that exhibit significant gravimetric hydrogen storage densities. However, despite being thermodynamically stable, these materials exhibit slow kinetics in hydrogen absorption and desorption processes. Experimental studies conducted by Anders Andreasen have examined the hydrogenation behaviors of Mg and Al alloys [17]. These studies have indicated that the inclusion of the Al element in the Mg/MgH_2 system significantly improves the kinetics of both hydrogenation and dehydrogenation reactions.

Researchers are exploring perovskite-type hydrides as promising solutions to these challenges [18–20]. These materials are appealing because they are lightweight, have stable complementary phases, and contain hydrogen atoms in interstitial sites that make hydrogen release easier. In particular, ternary perovskite hydrides (ABH_3) have attracted considerable attention for their potential use in hydrogen storage, rechargeable batteries, switchable mirrors, and other energy storage systems [21–26]. Owing to these exceptional features, numerous ABH_3 hydrides have been identified and experimentally examined by researchers as solid-state hydrogen storage materials. For instance, Masood et al. [27] investigated the hydrogen storage potential of Ge-based $XGeH_3$ (X = Mg, Ca, and Sr) perovskites, revealing their promising mechanical, thermoelectric, and electronic properties. Similarly, Kiani et al. [28] and Bakar et al. [29] conducted first-principles studies on $XGeH_3$ (X = K, Rb) and $XPtH_3$ (X = Cs, Fr) perovskites, highlighting their structural stability and electronic characteristics relevant to hydrogen storage. Furthermore, Azhar et al. [30] explored the properties of Rhodium-based $XRhH_3$ (X = Na, Cs, Sr) perovskites, emphasizing their optical and thermodynamic advantages. Rahman and Hossain explored $MCoH_3$ (M = Na, K, Rb) perovskite hydrides as potential candidates for hydrogen storage using density functional theory (DFT). Their results demonstrated that these compounds exhibit significant hydrogen storage capabilities in terms of both weight and volume, with $NaCoH_3$ achieving the highest performance at 3.56 wt% and 129.94 g H_2/L, respectively [31].

Researchers have recently focused extensively on Zr-based perovskite hydrides for hydrogen storage applications [19–24]. The $XZrH_3$ (X = Mg, Ca, Sr, Ba) cubic crystal structure and *Pm-3m* (#221) space group were analyzed, and gravimetric hydrogen storage capacities were found to be 2.55, 2.25, 1.66, and 1.31 wt%, respectively [32]. Similarly, Usman et al. [33] reported 2.93 wt% hydrogen storage capacity for $BeZrH_3$ perovskite hydrides with a desorption temperature of 336.62 K. Furthermore, Bahhar et al. [34] studied the structural, electronic, mechanical, optical, and hydrogen storage properties of $MgZrH_3$ perovskite hydride with 2.487 wt % hydrogen storage capacity using the GGA-PBE approach in the CASTEP package. More recently, Didi et al. [35] reported the desorption temperature and gravimetric hydrogen storage capacity of the $RbZrH_3$ compound as 548.15 K and 1.64 wt%, respectively, using first-principles calculations in CASTEP. Ahmad et al. studied the $ScZrH_3$ hydride and determined that it exhibited electrically metallic properties, its free hydrogen storage capacity was 2.86 wt% [36]. The favorable characteristics of zirconium, a transition metal, prompted us to explore Zr-based hydrides for hydrogen storage purposes. The presence of an unpaired electron in the Zr-4d state facilitates hydrogen absorption. Additionally, zirconium exhibits low density, efficient adsorption and desorption, kinetics, and strong thermodynamic stability. The hybridization of the Zr D-state with the s-state of alkali light metals further enhances its energy storage capabilities [37].

Despite the research on Zr-based perovskite hydrides, there is a chance to investigate new structures that might provide improved properties. In this study, DFT computations were used to thoroughly examine the mechanical, optoelectronic, anisotropic, and hydrogen storage properties of Zr-based perovskites $LiZrH_3$ and $KZrH_3$. By evaluating these fundamental properties, we aimed to provide a comprehensive understanding of the hydrogen storage potential of these materials. To our knowledge, these materials have been investigated for the first time, and there are no findings in literature, whether experimental or theoretical. The conclusions drawn from this research indicate a strong potential for influencing subsequent experimental and theoretical work concerning the hydride materials studied.

2. Methodology of calculation

The primary physical features of perovskite hydrides $LiZrH_3$ and $KZrH_3$, including elastic constants, dynamic, and hydrogen storage properties were initially examined using density functional theory (DFT) with the generalized gradient approximation (GGA-PBE) method [38]. All computations were conducted using VASP (Vienna Ab initio Simulation Package) [39,40], in which the projector-augmented wave (PAW) approach [41] to characterize the interactions between the cores of Li, K, Zr, and H atoms, and the valence electrons in this study. The valence-electron configurations used for Li, K, Zr, and H were $1s^2\ 2s^1$, $3s^2\ 3p^6\ 4s^1$, $4s^2\ 4p^6\ 4\ d^2\ 5s^2$, and $1s^1$, respectively. The energy-convergence criterion for geometric optimization was set to 10^{-8} eV/atom. The cut-off energy was set at 600 eV, and a k-points mesh of 12 x 12 ×12 in the first Brillouin zone was chosen for accurate computations [42]. Since the GGA-PBE method usually underestimates the band gap of materials, a more precise exchange-correlation functional, the Heyd-Scuseria-Ernzerhof (HSE06) functional, was used to explore the optoelectronic properties of $XZrH_3$ [43]. The ElasticPOST code [44] was employed to characterize the three-dimensional (3D) elastic anisotropic characteristics of these perovskite hydrides. Electron density distributions were visualized utilizing VESTA software [45]. The elastic constants were computed using the stress-strain method in VASP [46]. On the other hand, in the low-energy infrared region of the spectrum, optical simulations in metal and metal-like materials mostly reflect intraband contributions from conduction electrons [47]. Therefore, an empirical Drude term with a plasma frequency of 3 eV and damping of 0.05 eV was incorporated into the dielectric function for optical calculations. Phonon calculations for the $XZrH_3$ compounds, assuming a cubic structure with *Pm-3m* symmetry, were carried out using the supercell approach implemented in the PHONOPY code, with a 2 × 2 × 2 supercell [48].

3. Results and discussion

3.1. Structural properties

Perovskite hydrides $XZrH_3$, where X can be Lithium (Li) or Potassium (K), demonstrate remarkable stability in the cubic phase, characterized by the space group *Pm-3m* (no: 221). This structural stability is crucial for various applications, particularly in energy storage and conversion technologies [2]. Fig. 1 provides a detailed illustration of the crystal structure of cubic $XZrH_3$. In this configuration, the X atoms occupy the corners of the cubic unit cell at coordinates (0, 0, 0), while the zirconium (Zr) atoms are situated at the center of the cube at (0.5, 0.5, 0.5). The hydrogen (H) atoms are strategically placed at the face centers of the cube, located at (0.5, 0, 0.5), (0, 0.5, 0.5), and (0.5, 0.5, 0), effectively forming octahedral sites within the structure. This arrangement not only defines the geometric properties of the material but also plays a significant role in its chemical behavior and stability. Besides, determining the structural properties of these perovskite hydrides provides valuable

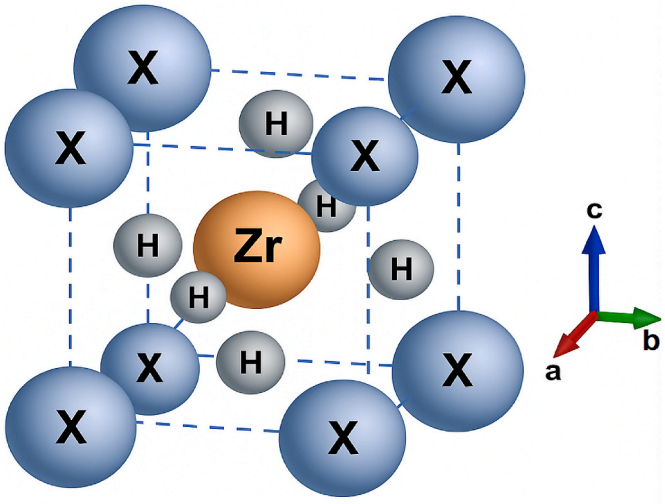

Fig. 1. Crystal structure of $XZrH_3$ perovskite type hydride.

information about the atomic arrangement and overall stability of the crystal structure. Understanding these properties is essential for predicting how the material will behave under various conditions, which is a focal point in material science. The relationship between energy and volume for the perovskite hydrides $XZrH_3$ (X = Li and K) is shown in Fig. 2. It highlights how the total energy of the system varies as a function of the unit cell volume. The parabolic curve observed in the energy versus volume plot is derived from the optimization of the crystal structure.

The Birch-Murnaghan equation of state [49] is employed to estimate the structural parameters obtained after this optimization process.

$$E_{tot}(V) = E_0(V) + \frac{BV}{B'}\left[\frac{\left(\frac{V_0}{V}\right)^{B'}}{B'-1}+1\right] - \frac{BV_0}{B'(B'-1)} \quad (1)$$

The symbols E_0, V, V_0, B, and B' denote the ground state energy, the volume of the unit cell, the optimized unit cell volume associated with the ground state energy, the bulk modulus, and the pressure derivative of the bulk modulus, respectively. Table 1 presents a comprehensive list of the optimized lattice constants (a), bulk modulus (B), the derivative of bulk modulus with respect to pressure (B'), and formation energy (ΔH_f). The optimized lattice constants for $LiZrH_3$ and $KZrH_3$ are observed to be 3.895 and 4.166 Å, respectively. This trend indicates an increase in

Table 1
The calculated lattice constant (a), Bulk modulus (B), pressure derivative of the Bulk modulus (B'), and formation enthalpy (ΔH_f) for $LiZrH_3$ and $KZrH_3$ hydrides.

Material	a (Å)	B (GPa)	B'	ΔH_f (eV/atom)
$LiZrH_3$	3.895	60.6	3.12	−0.645
$KZrH_3$	4.166	49.2	3.53	−0.561
$BeZrH_3$ [20]	3.80	59.80	–	−0.45
$MgZrH_3$ [21]	3.867	73.18	4.02	−0.871
$RbZrH_3$ [22]	4.23	46.12	3.62	−0.74
$LiSrH_3$ [36]	4.588	22.71	3.58	–

lattice constants, which can be attributed to the larger ionic radii of the elements involved. The bulk modulus quantifies a material's ability to withstand uniform compressive forces. When comparing the calculated values of bulk modulus in Table 1, $LiZrH_3$ (60.6 GPa) is larger than that of $KZrH_3$ (49.2 GPa). The calculated bulk modulus values of both materials are greater than 40 GPa, indicating that they are hard materials. These values are lower than those of $CaZrH_3$ (81.99 GPa) [32], $SrZrH_3$ (91.62 GPa) [32], and $MgZrH_3$ (73.18 GPa) [34], but higher than those of $RbZrH_3$ (46.12 GPa) [35], $KTiH_3$ (44.938 GPa) [50], and $LiSrH_3$ (22.71 GPa) [51].

A negative formation energy (ΔH_f) indicates that the compound is exothermic, meaning less energy is needed to break bonds than the energy released when new bonds are formed. It also shows whether the studied compound can be experimentally synthesized. The formation energy for these hydrides was calculated using the following equation:

$$\Delta H_f = \frac{E^{tot}_{XZrH_3} - \left(E^{tot}_X + E^{tot}_{Zr} + \frac{3}{2}E^{tot}_{H_2}\right)}{N} \quad (2)$$

where N is the total number of atoms in the system, E^{tot}_X, E^{tot}_{Zr}, and $E^{tot}_{H_2}$ stand for the ground state energies of the X, Zr, and H_2 atoms, respectively, and $E^{tot}_{XZrH_3}$ is the system's ground state energy. As shown in Table 1, the formation enthalpies per atom of $LiZrH_3$ and $KZrH_3$ are −0.645 eV and −0.561 eV, respectively, which indicates that $LiZrH_3$ is more stable than $KZrH_3$. This negative value indicates that these hydrides can be synthesized experimentally. Therefore, the calculated results are higher than the reported $BeZrH_3$ (−0.45 eV/atom) [33], $MgAlH_3$ (−0.499 eV/atom) [34], and $KTiH_3$ (−0.285 eV/atom) [50].

To evaluate the dynamic stability of the examined materials, an analysis of the phonon dispersion curves was conducted. Fig. 3 shows the phonon dispersion curves calculated along the high symmetry points in the first Brillouin zone. The presence of only real frequencies in a material's phonon spectrum indicates that it is dynamically stable; the

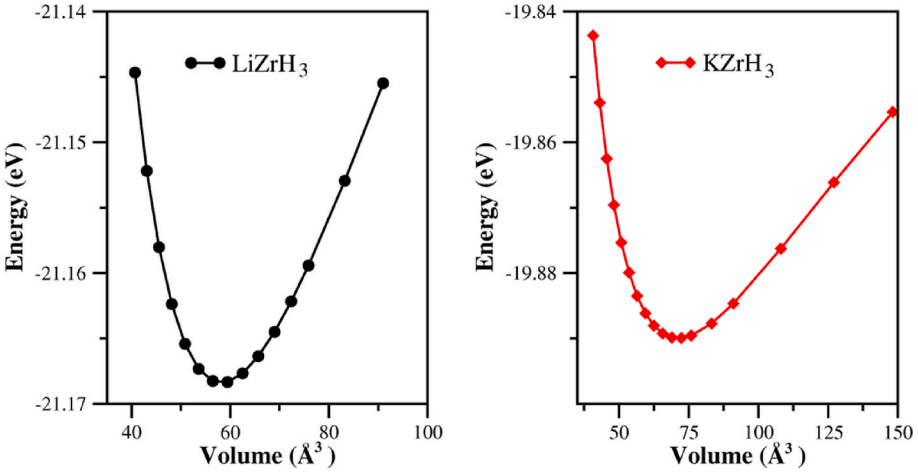

Fig. 2. The optimized total energy-volume curve for $LiZrH_3$ and $KZrH_3$ hydrides.

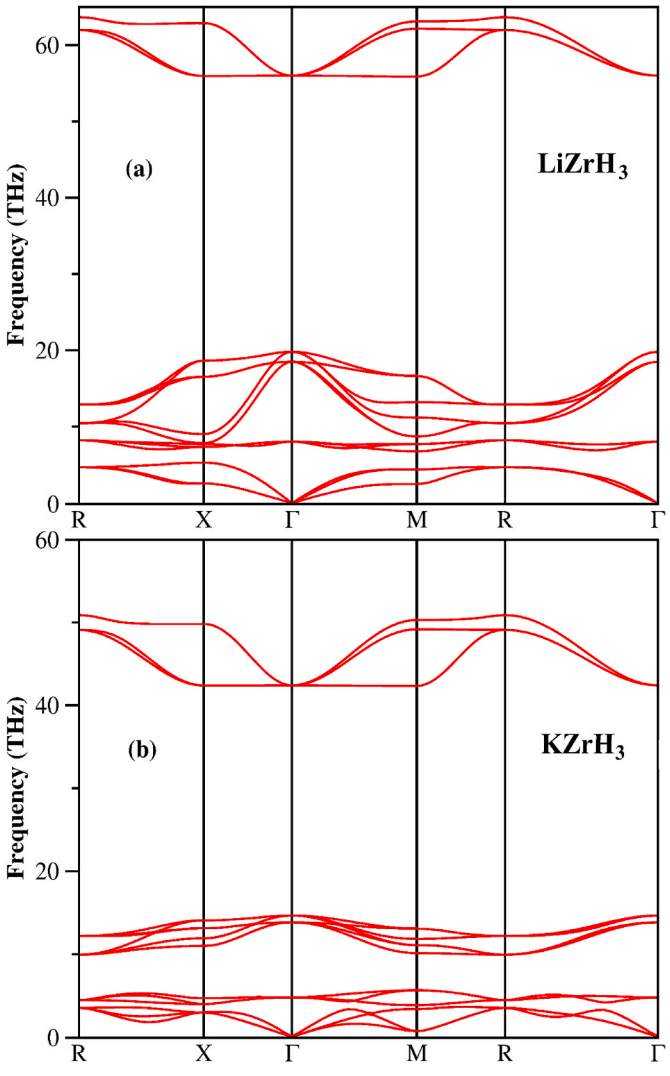

Fig. 3. The phonon dispersion curves (a) $LiZrH_3$, and (b) $KZrH_3$.

presence of imaginary frequencies, on the other hand, signifies dynamic instability. The lack of imaginary frequencies throughout the entire Brillouin zone shows that the $LiZrH_3$ and $KZrH_3$ compounds are dynamically stable.

3.2. Hydrogen storage properties

The use of hydrogen as a fuel is significantly hindered by the lack of suitable materials that have high gravimetric storage capacity, C_{wt} %. Greater gravimetric and volumetric hydrogen storage densities are crucial for the development of suitable materials for hydrogen storage applications. We have calculated the gravimetric and volumetric hydrogen storage densities of the perovskite-type hydrides $LiZrH_3$ and $KZrH_3$. To achieve this objective, the molar mass of the host material and the molar mass of hydrogen are utilized, and the subsequent mathematical relation is applied to compute C_{wt} % [52]:

$$C_{wt}\ (\%) = \frac{(H/M)m_H}{m_{host} + (H/M)m_H} \times 100\ \% \tag{3}$$

The variable H/M represents the ratio of hydrogen atoms to host atoms, while m_H and m_{host} denote the molar mass of hydrogen and the molar mass of the host material, respectively. As can be seen from Table 2, the gravimetric hydrogen storage densities for the hydrides $LiZrH_3$ and $KZrH_3$ are 2.99 % and 2.27 %, respectively. The hydrogen storage capacity of $LiZrH_3$ is superior to that of the $KZrH_3$ compound,

Table 2
The gravimetric (C_{wt}) and volumetric (ρ_{vol}) hydrogen storage capacity, desorption temperatures (T_{des}) of $LiZrH_3$ and $KZrH_3$ hydrides.

Material	C_{wt} (%)	ρ_{vol} (g.H_2/L)	T_{des} (K)
$LiZrH_3$	2.99	87.04	473.76
$KZrH_3$	2.27	72.80	421.06

and this suggests that $LiZrH_3$ may be a much more efficient material for hydrogen storage applications. The C_{wt} % values determined for $LiZrH_3$ and $KZrH_3$ are also higher than some of the perovskite hydrides previously reported for hydrogen storage applications, such as $CaZrH_3$ (2.25 %) [19], $RbZrH_3$ (1.64 %) [22], $CsTiH_3$ (1.65 %) [50].

Although these values remain below the DOE's 2025 target of 5.5 wt % for onboard hydrogen storage systems, it is important to emphasize that these materials demonstrate favorable thermodynamic stability, rapid hydrogen kinetics, and mechanical robustness. Such characteristics make them promise for alternative hydrogen storage applications, particularly in small-to medium-scale systems, such as stationary energy storage, backup power solutions, and hydrogen buffering in renewable energy setups, where high gravimetric capacity is not the sole performance criterion.

The volumetric hydrogen storage capacity refers to the amount of H_2 that can be stored per unit volume and is usually expressed in grams of H_2 per liter. The volumetric hydrogen storage capacity (ρ_{vol}) for $LiZrH_3$ and $KZrH_3$ was calculated using the formula below [53]:

$$\rho_{vol} = \frac{N_H \times m_H}{V\,(L) \times N_A} \tag{4}$$

In this equation, N_H, m_H, $V\,(L)$, and N_A denote the quantity of absorbed hydrogen, the molecular weight of hydrogen, the volume of the absorbent, and Avogadro's number, respectively. The calculated volumetric hydrogen storage capacities of these perovskite-type hydrides are listed in Table 2. Similar to the C_{wt} % result, $LiZrH_3$ (87.04 g.H_2/L) exhibits a larger ρ_{vol} compared to the other material $KZrH_3$ (72.80 g.H_2/L). The volumetric hydrogen storage capacity of $NaMTH_3$ (MT = Sc, Ti, V) in the Pm-3m crystal structure was reported as 80.47, 96.01, and 107.32 g.H_2/L, respectively [53]. Moreover, the desorption temperature of the perovskite-type hydrides can be determined using the following equation:

$$T_{des} = \frac{-\Delta H_f}{\Delta S} \tag{5}$$

where ΔS denotes the entropy change (for hydrogen, its value is 130.7 J/mol K) and T_{des} signifies the desorption temperature. As presented in Table 2, the calculated desorption temperatures for $LiZrH_3$ and $KZrH_3$ are 473.76 K and 421.06 K, respectively. The calculated desorption temperatures for the studied hydrides surpass room temperature (300 K), making them suitable for off-ship hydrogen storage applications [54].

3.3. Electronic properties

By examining the electronic band structures of a material, researchers can predict whether this material exhibits metallic, semiconducting, or insulating behavior. The electronic characteristics of $XZrH_3$ (X = Li and K) were analyzed using the HSE06 functional and the electronic band structures for these hydrides are displayed in Figs. 4 and 5, respectively, spanning an energy range from −8 eV to 6 eV. The red solid line, drawn horizontally at 0 eV, denotes the Fermi level (E_F). From these figures, it can be clearly seen that the conduction band overlaps with the valence band around the Fermi energy level, indicating that these perovskite-type hydrides have metallic characteristics. The metallic properties of materials present significant potential for applications in hydrogen storage [55]. The results obtained for these two materials are in agreement with previously reported materials $BeXH_3$ (X

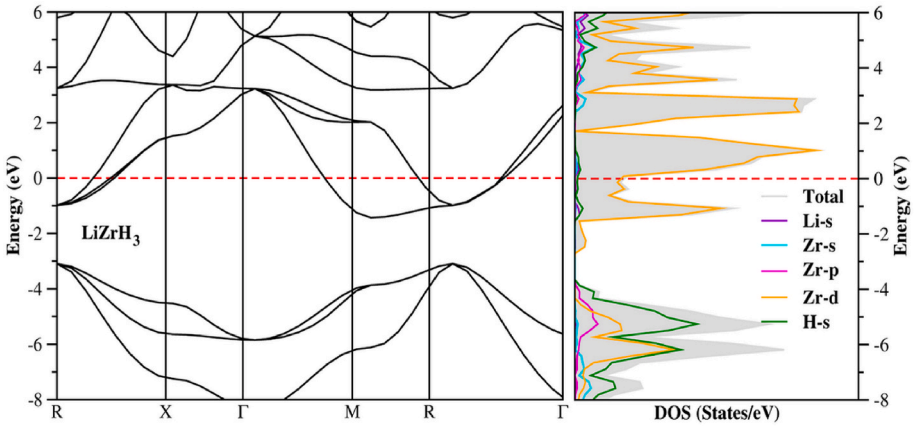

Fig. 4. The electronic band structure and TDOS-PDOS of $LiZrH_3$.

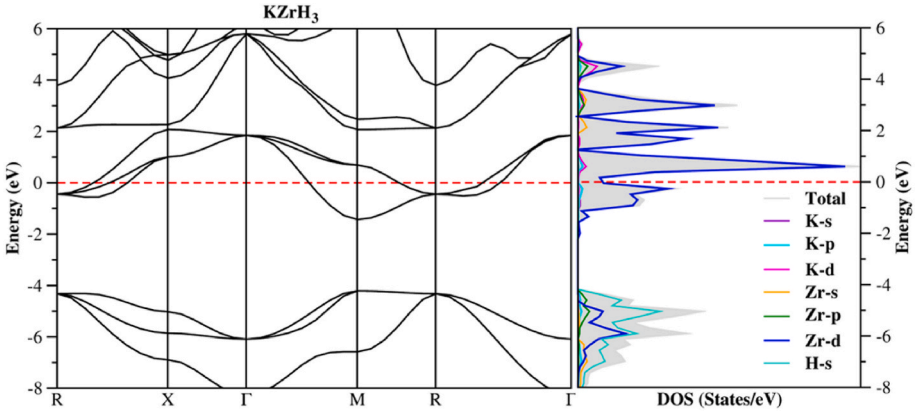

Fig. 5. The electronic band structure and TDOS-PDOS of $KZrH_3$.

= Ti, Zr) (metallic) [33], $MgXH_3$ (X = Al, Sc, and Zr) (metallic) [34], $RbZrH_3$ (metallic) [35], and $ScXH_3$ (X = Ti, Zr) (metallic) [36], etc.

Figs. 4 and 5 illustrate the total density of states (TDOS) alongside the corresponding projected density of states (PDOS) for the $LiZrH_3$ and $KZrH_3$, respectively. In the case of $LiZrH_3$, the highest density of states in the valence band is found at −5 eV, whereas in the conduction band, it peaks at 3 eV. This peak moves closer to the Fermi level for both $LiZrH_3$ and $KZrH_3$, as depicted in the figures. Similarly, $KZrH_3$ shows its peak density of states at −5 eV in the valence band and 1 eV in the conduction band. The presence of various peaks in the conduction band density of states indicates the peak arising from specific electron contributions at different energy levels, with pronounced peaks between 1 eV and 6 eV resulting from flattened bands in that energy interval. The largest contribution to total energy for $LiZrH_3$ and $KZrH_3$ comes from Zr-d orbitals both in the valence band and conduction band as shown in Figs. 4 and 5. Additionally, the electron density distribution function for

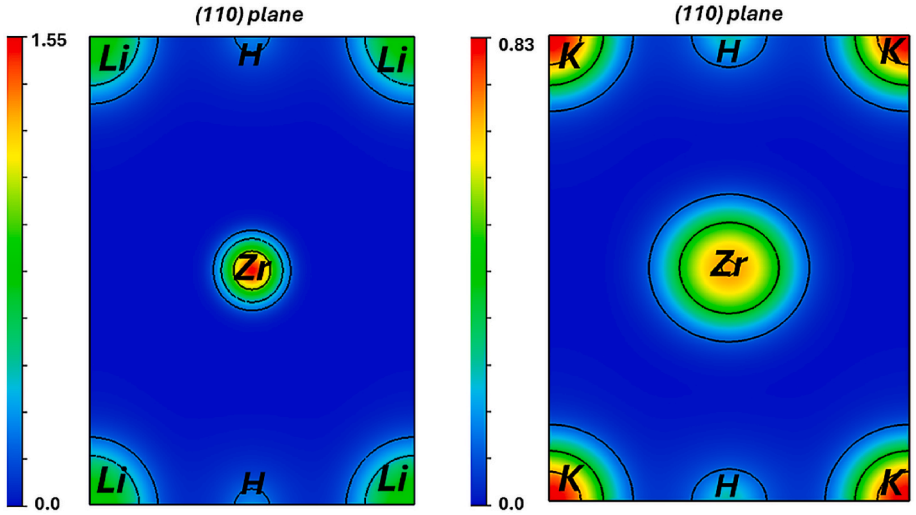

Fig. 6. Electron-density distribution (in units of e) for $LiZrH_3$ and $KZrH_3$ in (110) plane.

$LiZrH_3$ and $KZrH_3$ in the (110) plane was examined, as illustrated in Fig. 6. These figures illustrate the ionic bonding among the atoms of these materials. This result agrees with the results of Poisson's ratio in the mechanical properties section [30,56].

3.4. Optical properties

Optical properties often provide opportunities to enhance hardware performance across several applications, including photonics, optics, solar energy conversion, sensors, and hydrogen storage technologies. A deeper understanding of the interactions between hydrogen materials and the sun can be achieved by analyzing optical characteristics within the framework of hydrogen storage. The optical properties of the perovskite-type hydrides $XZrH_3$ (X = Li and K), with an in-depth calculation of various optical parameters such as dielectric function, conductivity, reflectivity, and absorption, were performed using the HSE06 functional [43]. Understanding the dielectric constant is crucial for probing the optical response of materials to incoming

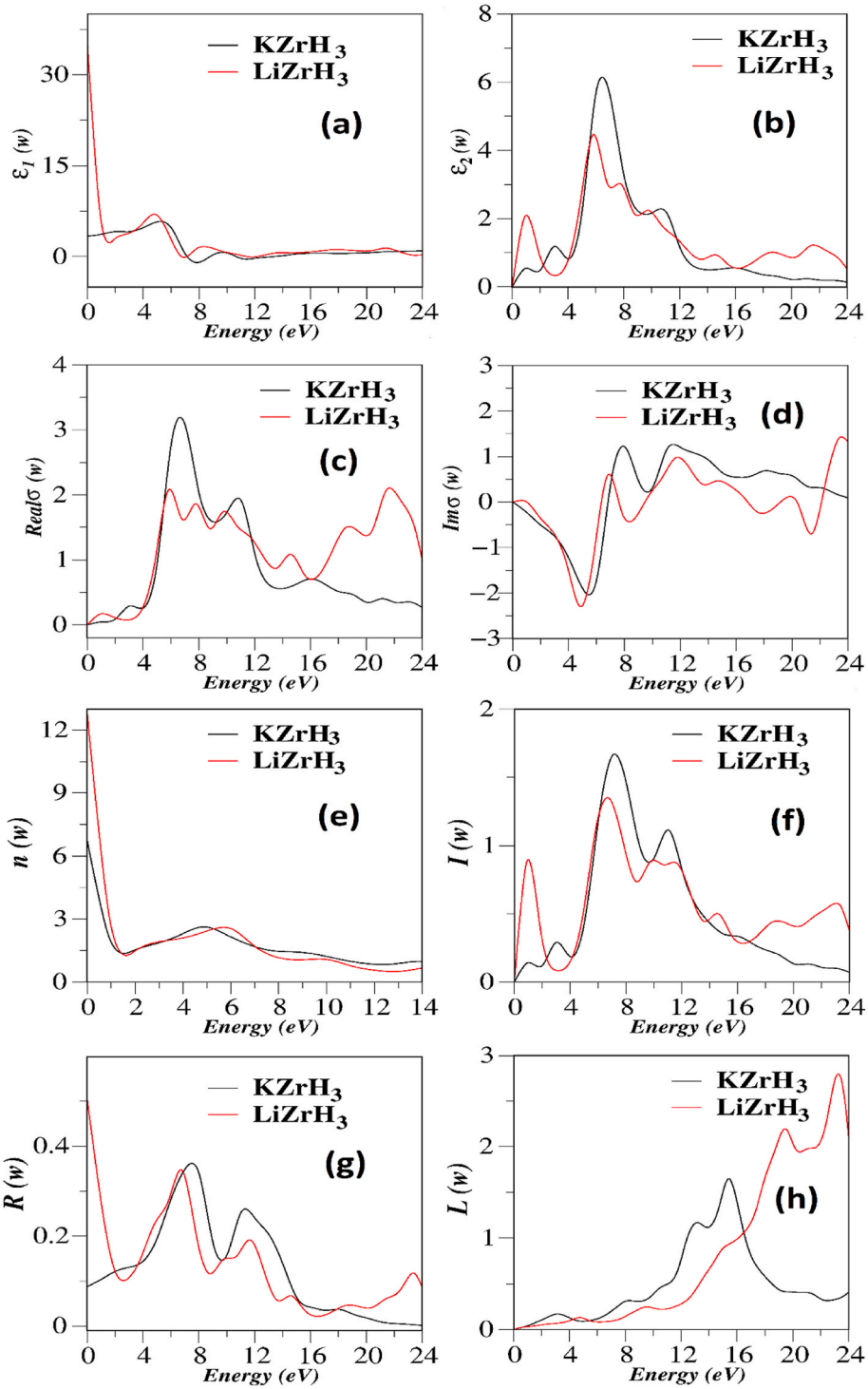

Fig. 7. Optical properties of $LiZrH_3$ and $KZrH_3$ (a) Real part of the dielectric function, (b) Imaginary part of the dielectric function, (c) Real part of optical conductivity, (d) Imaginary part of optical conductivity, (e) Refractive index, (f) Absorption coefficient, (g) Reflectivity and (h) Loss function.

electromagnetic radiation. The real and imaginary components of the dielectric constant, $\varepsilon(\omega)$, are derived using Kramer ' s-Kronig relations [57,58]. The equation for the real part of the dielectric constant, $\varepsilon_1(\omega)$, is given by:

$$\varepsilon(\omega) = \varepsilon_1(\omega) + i\varepsilon_2(\omega) \tag{6}$$

With the knowledge of $\varepsilon(\omega)$, one can easily calculate $\sigma(\omega)$ conductivity, $n(\omega)$ refractive index, $I(\omega)$ absorption coefficient, and $R(\omega)$ reflectivity using the sequential formulas given below [43]:

$$\sigma(\omega) = -\frac{i\omega}{4\pi}\varepsilon(\omega) \tag{7}$$

$$n(\omega) = \left[\frac{\sqrt{\varepsilon_1^2(\omega)+\varepsilon_2^2(\omega)}+\varepsilon_1(\omega)}{2}\right]^{1/2} \tag{8}$$

$$I(\omega) = \left[\frac{\sqrt{\varepsilon_1^2(\omega)+\varepsilon_2^2(\omega)}-\varepsilon_1(\omega)}{2}\right]^{1/2} \tag{9}$$

$$R(\omega) = \left|\frac{\sqrt{\varepsilon(\omega)}-1}{\sqrt{\varepsilon(\omega)}+1}\right|^2 \tag{10}$$

Fig. 7(a and b) depict the change of $\varepsilon_1(\omega)$ and $\varepsilon_2(\omega)$ for $LiZrH_3$ and $KZrH_3$ within the energy spectrum of 0–24 eV $\varepsilon_1(\omega)$ shows a sharp drop in the low-energy range, as seen in Fig. 7 (a). Moreover, $\varepsilon_1(\omega)$ tends to converge and progress parallel to the energy axis above 7 eV. This situation reflects the minimal polarization and dispersion of incident photons in this energy range [59,60]. The static dielectric constants $\varepsilon_1(0)$ for $LiZrH_3$ and $KZrH_3$ are measured as 35.01 and 3.39, respectively. The elevated positive values of $\varepsilon_1(0)$ signify a significant electrical energy storage capability and a considerable degree of polarization in these hydrides [60,61].

Fig. 7 (b) illustrates that the spectra of the imaginary component $\varepsilon_2(\omega)$ exhibit a significant peak in the ultraviolet range. The maximum value of $\varepsilon_2(\omega)$ was identified for $LiZrH_3$ at around 6.09 eV (4.25) and for $KZrH_3$ at roughly 6.24 eV, with a peak value of 6.11. Moreover, Fig. 7 (b) illustrates a subtle peak in the low-energy infrared region of the $\varepsilon_2(\omega)$ spectra for the two examined compounds. In the elevated energy range, $\varepsilon_2(\omega)$ attains nearly insignificant values and thereafter declines to zero beyond 12 eV. This signifies that the analyzed materials demonstrate negligible absorption and interference of electromagnetic radiation within this energy spectrum [62].

To investigate the conduction process in $XZrH_3$ (X = Li and K) hydrides, we have illustrated in Fig. 7(c and d) the variation of the real and imaginary parts of the optical conductivity as a function of energy. $KZrH_3$ is notable among these hydrides for its superior conductivity in the UV spectrum. The peak conductivity of $KZrH_3$ was determined to be 3.45 $(fs)^{-1}$, whereas $LiZrH_3$ exhibited a value of 2.22 $(fs)^{-1}$. In Fig. 7 (d), as the energy value increases, the imaginary components of $LiZrH_3$ and $KZrH_3$ attain their minimum values at 5 eV and 6 eV, respectively, before gradually rising, indicating a reduction in the reactive component of the material's reaction to an electric field.

The spectral variation of the refractive index $n(\omega)$ with energy for $XZrH_3$ (X = Li and K) is shown in Fig. 7 (e). As can be seen from Fig. 7 (a) and 7 (e), the patterns of the refractive index $n(\omega)$ and the real part of the dielectric function $\varepsilon_1(\omega)$ clearly coincide. For $LiZrH_3$ and $KZrH_3$, the static refractive index $n(0)$ has been determined to be 6.75 and 12.82, respectively. Additionally, the lower refractive index values occur at very high energies, suggesting that these hydrides are transparent to UV light.

The optical absorption coefficient of a substance is another crucial optical characteristic. This coefficient measures how well a material absorbs incident radiation. Fig. 7 (f) shows the absorption spectrum of $XZrH_3$ (X = Li and K) hydrides in the 0–24 eV range. The analysis reveals varying patterns in $I(\omega)$, with the most significant absorption peaks being 1.42 at 7.21 eV for $LiZrH_3$ and 1.67 at 7.75 eV for $KZrH_3$ compounds. The $KZrH_3$ compound has the largest value among the studied materials. The variable $I(\omega)$ plays a crucial role in energy storage and optoelectronics applications [63–65].

Reflectivity was used to assess the degree of light reflection at the surface of these materials. The reflectivity curves are presented in Fig. 7 (g). For these hydrides, the reflectivity demonstrates a pronounced decrease at very low energy, succeeded by smooth oscillations within the energy range of 2–14 eV. At 0 eV, $KZrH_3$ demonstrates the lowest reflectivity at 8.75 %, whereas $LiZrH_3$ displays the highest reflectivity at 50.53 %.

The possibility of photoelectron scattering is closely linked to the energy loss function, as illustrated in Fig. 7 (h). The peak energy loss values are 2.19 at 19.45 eV and 2.79 at 23.24 eV for $LiZrH_3$ and 1.64 at 15.44 eV for $KZrH_3$.

3.5. Mechanical properties

Mechanical stability is a crucial property that refers to a material's capacity to withstand deformation when subjected to various mechanical stresses and strains [54]. This concept encompasses the material's ability to endure fluctuations in both pressure and temperature, which are common in many practical applications. Additionally, mechanical stability involves the material's resistance to repeated cycles of adsorption and desorption, which is particularly relevant in contexts such as hydrogen storage, where materials must frequently transition between different states [54]. Therefore, a thorough investigation of the mechanical properties of these materials is extremely important for both scientific research and industrial applications.

For the mechanical stability of materials, the elastic constants must meet the Born stability criteria [66]. These criteria are critically important for ensuring the mechanical stability of materials and must remain below certain values for the material to be used safely. The Born criteria help us understand the elastic properties and durability of the material while also providing a foundation for the design and development of new hydrogen storage materials. The investigated materials have a cubic phase *Pm-3m* space group, and have three elastic stiffness tensors (C_{11}, C_{12}, and C_{44}). Born mechanical stability criteria for a cubic structure [67,68] are given as:

$$C_{11} > 0, \quad C_{11} - C_{12} > 0, C_{11} + 2C_{12} > 0, C_{44} > 0 \tag{11}$$

The analyzed materials conform to the Born stability criteria as presented in Table 3. $XZrH_3$ (X = Li and K) perovskite hydrides have been determined to be mechanically stable. The brittleness and ductility of these materials are determined using the Cauchy pressure (C_{12}-C_{44}) given in Table 3. The positive (negative) Cauchy pressure value can be used to infer the ductility (brittleness) [69]. As a result, it is uncovered that $KZrH_3$ is brittle while $LiZrH_3$ is ductile in nature.

Furthermore, these elastic constants facilitated the derivation of several mechanical parameters, including Bulk modulus, Shear modulus, Young's modulus, *B/G*, *G/B,* and Poisson's ratio, utilizing the Voigt, Reuss, and Hill methodologies [70–72]. For the $XZrH_3$ (X = Li and K) hydrides, the bulk modulus (B), shear modulus (G), and Young's modulus (E) were calculated using equations (12)–(17); the results are listed in Table 4.

$$B = \frac{1}{3}(C_{11} + 2C_{12}) \tag{12}$$

Table 3
Elastic constants (C_{ij}) and calculated Cauchy pressure (C_P) for $LiZrH_3$ and $KZrH_3$ hydrides.

Material	C_{11} (GPa)	C_{12} (GPa)	C_{44} (GPa)	C_P (GPa)
$LiZrH_3$	149.78	21.37	18.72	2.65
$KZrH_3$	102.65	31.72	35.01	−3.29

Table 4
The calculated values of Bulk modulus (B), Shear modulus (G), Young's modulus (E), B/G, G/B, and Poisson's ratio (ν) for $LiZrH_3$ and $KZrH_3$ perovskites.

Material	B (GPa)	G (GPa)	E (GPa)	B/G	G/B	ν
$LiZrH_3$	64.17	31.52	81.25	2.04	0.49	0.29
$KZrH_3$	55.36	35.19	87.12	1.57	0.64	0.24

$$G_V = \frac{1}{5}(3C_{44} - C_{12} + 3C_{11}) \tag{13}$$

$$G_R = \frac{(C_{11} - C_{12})5C_{44}}{4C_{44} + 3(C_{11} - C_{12})} \tag{14}$$

$$G = \frac{1}{2}(G_V + G_R) \tag{15}$$

$$E = \frac{9BG}{(G + 3B)} \tag{16}$$

$$\nu = \frac{1}{6}\left[\frac{3B - E}{B}\right] \tag{17}$$

The solidity of materials is explained by their Bulk modulus (B), which is 64.17 GPa for $LiZrH_3$ and 55.36 GPa for $KZrH_3$. $LiZrH_3$ exhibits the highest value among these hydrides, indicating low compression and strong stiffness [73]. Shear modulus (G) values for $LiZrH_3$ and $KZrH_3$ perovskites are 31.52 GPa and 35.19 GPa, respectively. Additionally, the bulk modulus of these hydrides is greater than the shear modulus, indicating that shear deformation primarily limits the mechanical strength. For $LiZrH_3$ and $KZrH_3$, the Young's moduli (E) are 81.25 GPa and 87.12 GPa, respectively. $KZrH_3$ is stiffer with a high degree of resistance. Therefore, from an engineering perspective, $KZrH_3$ may be more useful [74]. The computed results for B, G, and E are closely related to the reported materials, $MgZrH_3$ (B = 63.85, G = 35.79, and E = 90.31 GPa) [32], and $RbCdH_3$ (B = 57.33, G = 31.78, and E = 80.47 GPa) [75].

Two other indicators of a material's brittleness or ductility are Poisson's and Pugh's moduli. More precisely, a material is categorized as ductile if its Poisson's ratio is more than 0.26, if not, it is brittle. Conversely, a material is classified as ductile if its Pugh coefficient (B/G) is more than 1.75, if not, it is classified as brittle [75]. For $KZrH_3$, Poisson's and Pugh's ratios fall below the critical limits, whereas for $LiZrH_3$, they rise above the critical limits. This suggests that $KZrH_3$ exhibits brittleness, whereas $LiZrH_3$ exhibits ductility. According to the Cauchy pressure parameter, these outcomes are consistent.

Besides, Poisson's ratio (ν) may be calculated using Eq. (17), which relates to bonding properties of the materials. Numerous investigations indicate that covalent materials often have a Poisson's ratio of approximately 0.1, whereas ionic materials generally possess a Poisson's ratio of $\nu \geqslant 0.25$ [56]. As shown in Table 4, these investigated materials were found to be ionically bonded. At this point, the hydrides $XZrH_3$ (X = Li and K) are of ionic nature, and our results are in good agreement with the reported $XZrH_3$ (X = Mg, Ca, Sr, Ba) [19], $MgZrH_3$ [34], and $RbZrH_3$ [35]. Nonetheless, this is in line with the electron-density distribution analysis shown in Fig. 5 for the presented materials. On the other hand, the bonding type of the material is also determined by the G/B ratio; this ratio of around 1.1 (0.6) indicates covalent (ionic) bonding [56]. The G/B ratio for these $LiZrH_3$ and $KZrH_3$ hydrides was calculated as 0.49 and 0.64, respectively, indicating a notable occurrence of ionic bonding.

Additionally, other mechanical characteristics, including Debye temperature (Θ_D), average acoustic sound velocity (v_m), longitudinal velocity (v_l), transverse velocity (v_t), and melting temperature (T_M), have been computed for $XZrH_3$ (X = Li and K) and results are shown in Table 5, using the given equations below:

Table 5
The calculated density (ρ), longitudinal wave velocity (v_l), transverse wave velocity (v_t), average wave velocity (v_m), Debye temperature (θ_D), and melting temperature (T_M) of $LiZrH_3$ and $KZrH_3$.

Material	ρ (g/cm^3)	v_l (m/s)	v_t (m/s)	v_m (m/s)	θ_D (K)	T_M
$LiZrH_3$	2.912	6039	3290	3670	483.5	1438
$KZrH_3$	3.210	5645	3311	3671	455.7	1160

$$\Theta_D = \frac{h}{k}\sqrt[3]{\frac{3n}{4\pi}\left(\frac{N_A\rho}{M}\right)}v_m \tag{18}$$

$$v_m = \sqrt[3]{\frac{1}{3}\left(\frac{2}{v_t^3} + \frac{1}{v_l^3}\right)} \tag{19}$$

$$v_l = \sqrt{\frac{3B + 4G}{3\rho}} \tag{20}$$

$$v_t = \sqrt{\frac{G}{\rho}} \tag{21}$$

$$T_M = \left[553 + \left(\frac{5.91 * C_{11}}{GPa}\right)\right]K \mp 300K \tag{22}$$

The Debye temperature (Θ_D) of $LiZrH_3$ is greater than that of $KZrH_3$ because it has stronger internal bonding. The present findings are higher than the published values for $SrZrH_3$ (374.37 K) [19], $BaZrH_3$ (222.64 K) [32], and $MgAlH_3$ (427.53 K) [34]. Furthermore, the melting temperature decreases as the density of these materials increases, indicating a correlation with the rising elastic constants [56]. There is an observed linear correlation between the melting temperature and the Debye temperature of these perovskite structures. This phenomenon is elucidated by the rise in the ionic radius of the cation from Li to K.

3.6. Anisotropy properties

The anisotropy factor (A) serves as a crucial parameter for evaluating the elastic anisotropy of a given compound. This factor allows researchers and engineers to understand how the material's mechanical properties vary with direction. Specifically, the anisotropy factors associated with the principal crystallographic planes, namely the (1 0 0), (0 1 0), and (0 0 1) directions, can be denoted as A_1, A_2, and A_3, respectively. By analyzing these factors, one can gain insights into the directional dependence of the material's elastic behavior, which is essential for applications that require precise mechanical performance under varying stress conditions. Understanding these anisotropy factors is vital for optimizing material selection and engineering designs in various fields, from aerospace to civil engineering [76]. The elastic anisotropy of a cubic crystal can be quantified using various anisotropy indices, such as the universal anisotropy index (A^U), the Zener anisotropy index (A^Z), and the percentage anisotropies in compression (A^B) and shear (A^G). These indices can be determined using the formulas provided in Refs. [77–80] and are listed in Table 6.

$$A^U = 5\frac{G_V}{G_R} + \frac{B_V}{B_R} - 6 \tag{23}$$

$$A_1 = A_2 = A_3 = A^Z = \frac{2C_{44}}{(C_{11} - C_{12})} \tag{24}$$

$$A^B = \frac{(B_V - B_R)}{(B_V + B_R)}\ X\ 100\% \tag{25}$$

$$A^G = \frac{(G_V - G_R)}{(G_V + G_R)}\ X\ 100\% \tag{26}$$

Table 6
Anizotropy parameters.

Material	B_V (GPa)	B_R (GPa)	G_V (GPa)	G_R (GPa)	B_V/B_R	G_V/G_R	A^U	A^Z	A_G	A_B
$LiZrH_3$	64.17	64.17	36.91	26.12	1.00	1.41	2.05	0.29	17.12	0
$KZrH_3$	55.36	55.36	35.20	35.18	1.00	1.00	0	0.98	0.03	0

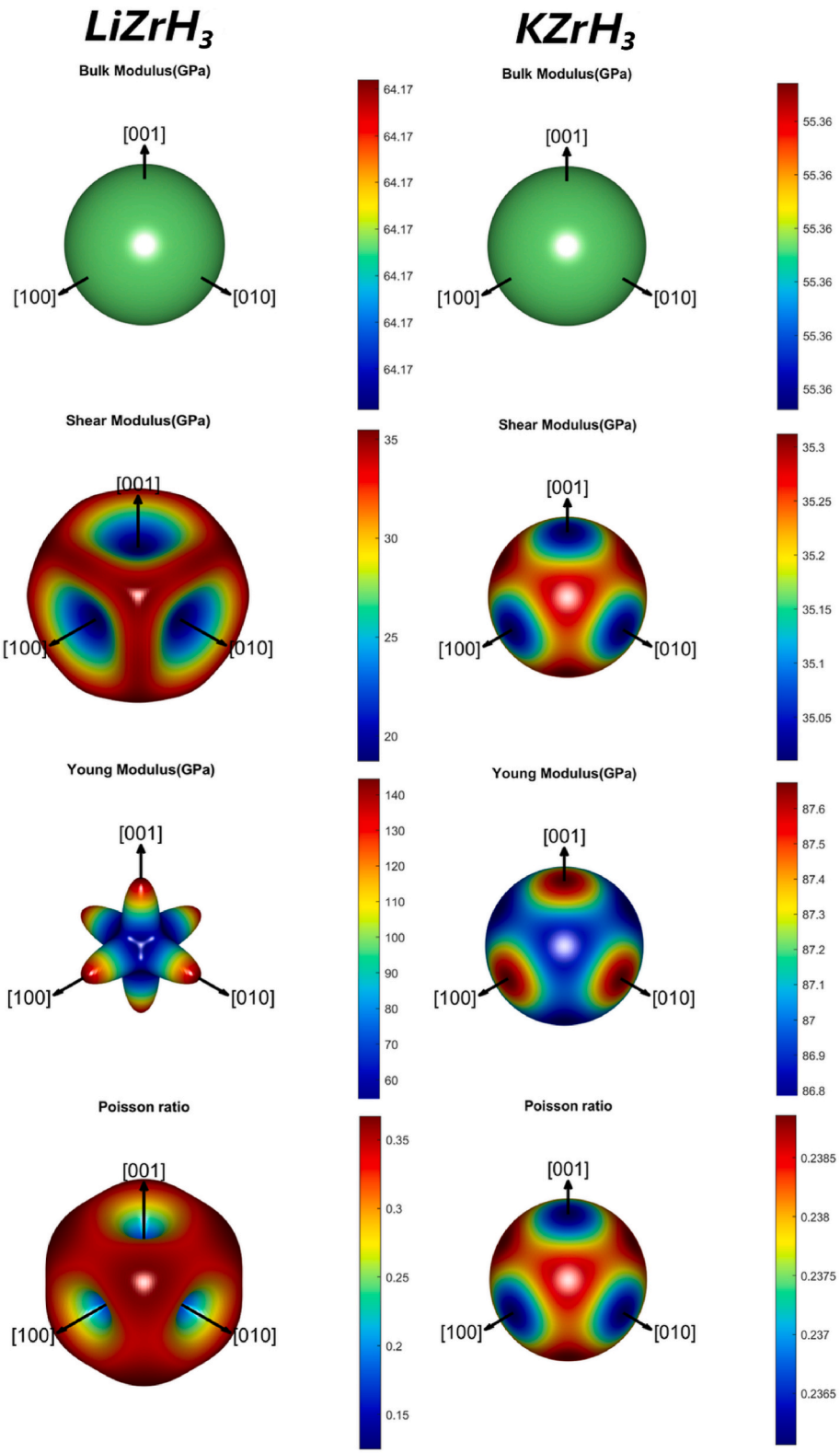

Fig. 8. Three-dimensional view of B, ν, G, and E parameters of $LiZrH_3$ and $KZrH_3$. Nonspherical geometries for B, ν, G, and E prove the presence of elastic anisotropy.

In the above equations, B_V (G_V) and B_R (G_R) refer to the Voigt and Reuss estimates for Bulk (Shear moduli), respectively. Additionally, C_{11}, C_{12}, and C_{44} are three independent constants that are found in cubic crystals. The universal anisotropy factor (A^U) can assume values zero or positive. A value of zero for A^U indicates that the crystal is isotropic, while any value greater than zero signifies the existence of anisotropy. The universal anisotropy factors for $LiZrH_3$ and $KZrH_3$ are 2.05 and 0, respectively, as shown in Table 6. This implies that $LiZrH_3$ shows anisotropy while $KZrH_3$ is isotropic. For an isotropic crystal, $A^G = 0$ and $A^B = 0$. Any deviation from zero implies the degree of anisotropy. In our work $A^B = 0$ both for $LiZrH_3$ and $KZrH_3$. As seen from Table 6, $A^G = 17.12$ for $LiZrH_3$ and $A^G = 0.03$ for $KZrH_3$ which states that the studied hydrides are isotropic in compression and anisotropic in shear.

The ElasticPOST code [44] was used to visualize the effect of anisotropy on mechanical properties in 3D. Fig. 8 presents the colored 3D view of B, ν, G, and E parameters for $LiZrH_3$ and $KZrH_3$ in [100], [010], and [001] planes. The variations from a perfect sphere in the figures generated using the ElasticPOST code reflect the level of anisotropy in the three-dimensional mechanical properties. Fig. 8 illustrates that the 3D projections of the E, G, and ν values for $LiZrH_3$ do not form a perfectly spherical shape. In contrast, the E, G, and ν values for $KZrH_3$ are nearly isotropic. In Table 7, the calculated maximum and minimum values of E, G, and ν are given. By dividing the relevant parameters , we obtain the anisotropy for $LiZrH_3$ as 3.43, 2.82, and 11.95. Similarly, we obtain the anisotropy for $KZrH_3$ as 1.01, 1.01, and 1.03. Consequently, the numerical values of elastic anisotropy tabulated in Table 7 and the 3D analysis (Fig. 8) corroborate with each other in terms of the elastic anisotropy properties of the $XZrH_3$ (X = Li and K).

Table 7
The calculated minimum and maximum values of Shear modulus (G), Young's modulus (E), and Poisson's ratio (ν) of $LiZrH_3$ and $KZrH_3$ perovskite hydrides.

Material	Young's Modulus		Shear Modulus		Poisson's Ratio	
	E_{min}	E_{max}	G_{min}	G_{max}	ν_{min}	ν_{max}
$LiZrH_3$	18.72	64.21	51.18	144.44	0.05	0.63
Anisotropy	3.43		2.82		11.95	
$KZrH_3$	35.01	35.47	86.75	87.67	0.23	0.24
Anisotropy	1.01		1.01		1.03	

4. Conclusions

This study employed first-principles calculations using the DFT method within the VASP software to investigate the structural, electronic, optical, and mechanical properties of Zr-based perovskites, $XZrH_3$ (X = Li and K), for hydrogen storage applications. The negative formation enthalpies of both compounds confirm their thermodynamic stability and synthetic feasibility. Additionally, Born's stability criterion was used to verify the mechanical stability of these hydrides. Besides, the absence of imaginary frequencies in $XZrH_3$ indicates that these compounds are entirely dynamically stable. Analysis of the band structure and density of states (DOS) indicated metallic behavior in these materials. $LiZrH_3$ was found to be ductile, whereas $KZrH_3$ exhibited brittleness. The optical properties were thoroughly examined related to photon energy, revealing that $KZrH_3$ is the most conductive material in the ultraviolet spectrum. The gravimetric hydrogen storage capacity and desorption temperatures were determined to be 2.99 wt% at 473.76 K for $LiZrH_3$ and 2.27 wt% at 421.06 K for $KZrH_3$. The results suggest that $XZrH_3$ perovskites have considerable potential for use as metal hydrides in hydrogen storage applications. Nonetheless, more theoretical and experimental investigations are necessary to enhance the features of these structures.

CRediT authorship contribution statement

A. Candan: Writing – original draft, Visualization, Validation, Software, Methodology, Investigation, Formal analysis, Data curation. **S. Akbudak:** Writing – original draft, Visualization, Methodology, Investigation, Conceptualization.

Declaration of competing interest

The authors declare the following financial interests/personal relationships which may be considered as potential competing interests: Abdullah Candan reports was provided by Kirsehir Ahi Evran University. If there are other authors, they declare that they have no known competing financial interests or personal relationships that could have appeared to influence the work reported in this paper.

References

[1] Kuo MH, Neykova N, Stachiv I. Overview of the recent findings in the perovskite-type structures used for solar cells and hydrogen storage. Energies 2024;17(18):4755. https://doi.org/10.3390/en17184755.
[2] Sun C, Alonso JA, Bian J. Recent advances in perovskite-type oxides for energy conversion and storage applications. Adv Energy Mater 2021;11(2):2000459. https://doi.org/10.1002/aenm.202000459.
[3] Kostopoulou A, Brintakis K, Nasikas NK, Stratakis E. Perovskite nanocrystals for energy conversion and storage. Nanophotonics 2019;8(10):1607–40. https://doi.org/10.1515/nanoph-2019-0119.
[4] Tufail D, Ahmed U, Haleem M, Amin B, Shafiq M. DFT study of alkaline earth metals $NaXH_3$ (X= Be, Mg, Ca, Sr) for hydrogen storage capacity. RSC Adv 2025;15(1):337–47. https://doi.org/10.1039/D4RA05327C. 2025.
[5] Bosu S, Rajamohan N. Recent advancements in hydrogen storage-Comparative review on methods, operating conditions and challenges. Int J Hydrogen Energy 2024;52:352–70. https://doi.org/10.1016/j.ijhydene.2023.01.344.
[6] Xu Y, Zhou Y, Li Y, Ding Z. Research progress and application prospects of solid-state hydrogen storage technology. Molecules 2024;29(8):1767. https://doi.org/10.3390/molecules29081767.
[7] Hisham SM, Sazali N, bin Kamarulzaman MK. Exploring hydrogen storage options: a brief review of gaseous, liquid, and solid-state approaches. Eng Technol Appl Sci Res 2024;14(5):16580–5. https://doi.org/10.48084/etasr.7039.
[8] Xu Y, Zhou Y, Li Y, Ding Z. Carbon-based materials for Mg-based solid-state hydrogen storage strategies. Int J Hydrogen Energy 2024;69:645–59. https://doi.org/10.1016/j.ijhydene.2024.05.044.
[9] Bishnoi A, Pati S, Sharma P. Architectural design of metal hydrides to improve the hydrogen storage characteristics. J Power Sources 2024;608:234609. https://doi.org/10.1016/j.jpowsour.2024.234609.
[10] Wang Y, Xue Y, Züttel A. Nanoscale engineering of solid-state materials for boosting hydrogen storage. Chem Soc Rev 2024;53(2):972. https://doi.org/10.1039/D3CS00706E.
[11] Hong H, Guo H, Cui Z, Ball A, Nie B. Structure modification of magnesium hydride for solid hydrogen storage. Int J Hydrogen Energy 2024;78:793–804. https://doi.org/10.1016/j.ijhydene.2024.06.327.
[12] Franco A, Giovannini C. Hydrogen gas compression for efficient storage: balancing energy and increasing density. Hydrogen 2024;5(2):293–311. https://doi.org/10.3390/hydrogen5020017.
[13] Alssalehin E, Holborn P, Pilidis P. Assessment of hydrogen storage and pipelines for hydrogen farm. Energies 2025;18(5):1167. https://doi.org/10.3390/en18051167.
[14] Duartey KO, Ampomah W, Rahnema H, Mehana M. Underground hydrogen storage: transforming subsurface science into sustainable energy solutions. Energies 2025;18(3):1–32. https://doi.org/10.3390/en18030748.
[15] Ma N, Zhao W, Wang W, Li X, Zhou H. Large scale of green hydrogen storage: opportunities and challenges. Int J Hydrogen Energy 2024;50:379–96. https://doi.org/10.1016/j.ijhydene.2023.09.021.
[16] Niaz S, Manzoor T, Pandith AH. Hydrogen storage: materials, methods and perspectives. Renew Sustain Energy Rev 2015;50:457–69. https://doi.org/10.1016/j.rser.2015.05.011.
[17] Andreasen A. Hydrogenation properties of Mg–Al alloys. Int J Hydrogen Energy 2008;33(24):7489–97. https://doi.org/10.1016/j.ijhydene.2008.09.095.
[18] Lavanya M, Shrivastava S, Lakshmi T, Sandadi ER, Gour S, Thomas NA, Priya SS, Sudhakar K. An overview of hydrogen storage technologies–Key challenges and opportunities. Mater Chem Phys 2024;325:129710. https://doi.org/10.1016/j.matchemphys.2024.129710.
[19] Bosu S, Rajamohan N. Recent advancements in hydrogen storage - comparative review on methods, operating conditions and challenges. Int J Hydrogen Energy 2024;52:352–70. https://doi.org/10.1016/j.ijhydene.2023.01.344.
[20] Yue M, Lambert H, Pahon E, Roche R, Jemei S, Hissel D. Hydrogen energy systems: a critical review of technologies, applications, trends and challenges. Renew Sustain Energy Rev 2021;146:111180. https://doi.org/10.1016/j.rser.2021.111180.
[21] Schouwink P, Ley MB, Tissot A, Hagemann H, Jensen TR, Smrčok Ľ, Černý R. Structure and properties of complex hydride perovskite materials. Nat Commun 2014;5(1):5706. https://doi.org/10.1038/ncomms6706. 2014.
[22] Zhang W, Eperon GE, Snaith HJ. Metal halide perovskites for energy applications. Nat Energy 2016;1(6):16048. https://doi.org/10.1038/nenergy.2016.48.

[23] Hayat S, Arif Khalil RM, Hussain MI, Rana AM, Hussain F. Ab-initio study of the structural, optoelectronic, magnetic, hydrogen storage properties and mechanical behavior of novel combinations of hydride perovskites $LiXH_3$ (X=Cr, Fe, Co, & Zn) for hydrogen storage applications. J Comput Electron 2021;20:2284–99. https://doi.org/10.1007/s10825-021-01807-3.
[24] Usman M, Wu A, Bibi N, Rehman S, Rehman MA, Ahmad S, et al. Hydrogen storage application of Zn-based hydride-perovskites: a computational insight. Opt Quant Electron 2024;56(9):1478. https://doi.org/10.1007/s11082-024-07399-z.
[25] Shahzad MK, Hussain S, Khan MN, Aslam MJ, Mohammed RM, Tirth V, et al. Computational insights of double perovskite Na_2CaCdH_6 hydride alloy for hydrogen storage applications: a DFT investigation. Sci Rep 2024;14(1):25102. https://doi.org/10.1038/s41598-024-76062-0.
[26] Konysheva E, Irvine JT. Thermochemical and structural stability of A- and B-Site-Substituted perovskites in hydrogen-containing atmosphere. Chem Mater 2009;21(8):1514–23. https://doi.org/10.1021/cm802996p.
[27] Masood M, Murtaza G, Ahmad N, Touqir M, Hafiz I, Usman A, et al. An ab-initio study of the physical properties of Ge-based perovskites $XGeH_3$ (X=Mg, Ca, and Sr) for potential hydrogen storage application. Int J Hydrogen Energy 2025;97:981–93. https://doi.org/10.1016/j.ijhydene.2024.11.470.
[28] Kiani MS, Bakar A, Rehman E. First-principles study on structural, elasto-mechanical, electronic, thermodynamic and hydrogen storage properties of $XGeH_3$ (X=K, Rb) hydrides. Results Phys 2025;68:108078. https://doi.org/10.1016/j.rinp.2024.108078.
[29] Bakar A, Muhammad H, Ahmed M, Kiani MS, Quader A, Batay S, Ali HE. Investigations for hydrogen storage applications of $XPtH_3$ (X = Cs, Fr) hydrides: a first principles study. Chem Phys 2025;591:112566. https://doi.org/10.1016/j.chemphys.2024.112566.
[30] Azhar U, Iftikhar MT, Arif M, Rehman MA, Ibrahim TH, El-Kadri OM. First principle investigation on the physical properties of rhodium-based $XRhH_3$ (X= Na, Cs or Sr) perovskites hydride for hydrogen storage applications. Int J Hydrogen Energy 2025;101:1448–59. https://doi.org/10.1016/j.ijhydene.2024.12.366.
[31] Rahman MA, Hossain AA. Investigating the physical and hydrogen storage properties of alkali metal-based cobalt hydrides. Int J Hydrogen Energy 2025;97:457–68. https://doi.org/10.1016/j.ijhydene.2024.11.441.
[32] Masood MK, Khan W, Bibi S, Khan N, Pingak RK, Tahir K, et al. The structural, elastic, optoelectronic properties and hydrogen storage capability of lead-free hydrides $XZrH_3$ (X: Mg/Ca/Sr/Ba) for hydrogen storage application: a DFT study. Comput Theor Chem 2024;1242:114941. https://doi.org/10.1016/j.comptc.2024.114941.
[33] Usman M, Bibi N, Rahman S, Rehman MA, Ahmad S. A DFT study to investigate $BeXH_3$ (X= Ti, Zr) hydride perovskites for hydrogen storage application. Comput Theor Chem 2024;1240:114820. https://doi.org/10.1016/j.comptc.2024.114820.
[34] Bahhar S, Tahiri A, Jabar A, Louzazni M, Idiri M, Bioud H. Computational assessment of $MgXH_3$ (X= Al, Sc and Zr) hydrides materials for hydrogen storage applications. Int J Hydrogen Energy 2024;58:259–67. https://doi.org/10.1016/j.ijhydene.2024.01.176.
[35] Didi Y, Bahhar S, Tahiri A, Naji M, Rjeb A. A computational study of metal hydrides based on rubidium for developing solid-state hydrogen storage. Chem Select 2024;9(22):e202401444. https://doi.org/10.1002/slct.202401444.
[36] Ahmad S, Tabassum M, Bibi N, Rehman S, Masood MK, Zulfiqar M. Exploring Sc-Based Hydride Perovskites $Scxh_3$ (X= Ti, Zr) Using First Principles: A Novel Pathway for Efficient Hydrogen Storage. Available at SSRN 5074126, https://dx.doi.org/10.2139/ssrn.5074126; 2024.
[37] Gupta SL, Kumar S, Panwar S. Ab initio studies of newly proposed zirconium based novel combinations of hydride perovskites $ZrXH_3$ (X= Zn, Cd) as hydrogen storage applications. Int J Hydrogen Energy 2024;55:1465–75. https://doi.org/10.1016/j.ijhydene.2023.11.286.
[38] Perdew JP, Burke K, Ernzerhof M. Generalized gradient approximation made simple. Phys Rev Lett 1996;77(18):3865–8. https://doi.org/10.1103/PhysRevLett.78.1396.
[39] Kresse G, Hafner J. Ab initio molecular dynamics for liquid metals. Phys Rev B 1993;47:558–61. https://doi.org/10.1103/PhysRevB.47.558.
[40] Kresse G, Furthmuller J. Efficiency of ab initio total energy calculations for metals and semiconductors using a plane-wave basis set. Comput Mater Sci 1996;6:15–50. https://doi.org/10.1016/0927-0256(96)00008-0.
[41] Blöchl PE. Projector augmented-wave method. Phys Rev B 1994;50:17953–79. https://doi.org/10.1103/PhysRevB.50.17953.
[42] Monkhorst HJ, Pack JD. Special points for Brillouin-zone integrations. Phys Rev B 1976;13(12):5188. https://doi.org/10.1103/PhysRevB.13.5188.
[43] Paier J, Marsman M, Hummer K, Kresse G, Gerber IC, Ángyán JG. Screened hybrid density functionals applied to solids. J Chem Phys 2006;124(15):154709. https://doi.org/10.1063/1.2187006.
[44] Liao M, Liu Y, Cui P, Qu N, Zhou F, Yang D, et al. Modeling of alloying effect on elastic properties in BCC Nb-Ti-V-Zr solid solution: from unary to quaternary. Comput Mater Sci 2020;172:109289. https://doi.org/10.1016/j.commatsci.2019.109289.
[45] Momma K, Izumi F. VESTA 3 for three-dimensional visualization of crystal, volumetric and morphology data. J Appl Crystallogr 2011;44(6):1272–6. https://doi.org/10.1107/S0021889811038970.
[46] Le Page Y, Saxe P. Symmetry-general least-squares extraction of elastic data for strained materials from ab initio calculations of stress. Phys Rev B 2002;65(10):104104. https://doi.org/10.1103/PhysRevB.65.104104.
[47] Li X, Cui H, Zhang R. First-principles study of the electronic and optical properties of a new metallic MoAlB. Sci Rep 2016;6(1):39790. https://doi.org/10.1038/srep39790.
[48] Togo A, Oba F, Tanaka I. First-principles calculations of the ferroelastic transition between rutile-type and $CaCl_2$-type SiO_2 at high pressures. Phys Rev B 2008;78(13):134106. https://doi.org/10.1103/PhysRevB.78.134106.
[49] Birch F. Finite elastic strain of cubic crystals. Phys Rev 1947;71:809–24. https://doi.org/10.1103/PhysRev.71.809.
[50] Xu N, Chen Y, Chen S, Li S, Zhang W. First-principles investigation for the hydrogen storage properties of $XTiH_3$ (X= K, Rb, Cs) perovskite type hydrides. Int J Hydrogen Energy 2024;50:114–22. https://doi.org/10.1016/j.ijhydene.2023.06.254. 2024.
[51] Raza HH, Murtaza G, Khalil RMA. Optoelectronic and thermal properties of $LiXH_3$ (X= Ba, Sr and Cs) for hydrogen storage materials: a first principle study. Solid State Commun 2019;299:113659. https://doi.org/10.1016/j.ssc.2019.113659. 2019.
[52] Ahmed M, Bakar A, Orynbassar A, Shynarbek N, Tahir MA, Shalenov EO, Ibraheem AA. First principles investigations of Lithium based hydrides $LiXH_3$ (X= Al, Ga, In) for hydrogen storage applications. Int J Hydrogen Energy 2025;98:25–34. https://doi.org/10.1016/j.ijhydene.2024.11.409.
[53] Ur Rehman Z, Rehman MA, Alomar SY, Rehman B, Awais M, Amjad M, et al. Hydrogen storage capacity of lead-free perovskite $NaMTH_3$ (MT= Sc, Ti, V): a DFT study. Int J Hydrogen Energy 2024;(1):4009198. https://doi.org/10.1155/2024/4009198.
[54] Ayyaz A, Ullah MA, Zaman M, Alkhaldi ND, Mahmood Q, Boukhris I, et al. Investigation of hydrogen storage and energy harvesting potential of double perovskite hydrides A_2LiCuH_6 (A= Be/Mg/Ca/Sr): a DFT approach. Int J Hydrogen Energy 2025;102:1329–39. https://doi.org/10.1016/j.ijhydene.2025.01.117.
[55] Saharan S, Ghanekar U, Meena S. V_2N MXene for hydrogen storage: first-principles calculations. J Phys Chem C 2024;128(4):1612–20. https://doi.org/10.1021/acs.jpcc.3c07786.
[56] Khan W. Computational screening of $BeXH_3$ (X: Al, Ga, and In) for optoelectronics and hydrogen storage applications. Mater Sci Semicond Process 2024;174:108221. https://doi.org/10.1016/j.mssp.2024.108221.
[57] Marius G. The physics of semiconductors: kramers-Kronig relations. Berlin Heidelberg: Springer; 2010. p. 775–6. https://doi.org/10.1007/978-3-642-13884-3_26.
[58] Candan A, Kushwaha AK. A first-principles study of the structural, electronic, optical, and vibrational properties for paramagnetic half-Heusler compound TiIrBi by GGA and GGA+ mBJ functional. Mater Today Commun 2021;27:102246. https://doi.org/10.1016/j.mtcomm.2021.102246.
[59] Khalil RM, Hayat S, Hussain MI, Rana AM, Hussain F. DFT based first principles study of novel combinations of perovskite-type hydrides $XGaH_3$ (X= Rb, Cs, Fr) for hydrogen storage applications. AIP Adv 2021;11(2). https://doi.org/10.1063/5.0037790.
[60] Siddique A, Khalil A, Almutairi BS, Tahir MB, Sagir M, Ullah Z, et al. Structures and hydrogen storage properties of $AeVH_3$ (Ae=Be, Mg, Ca, Sr) perovskite hydrides by DFT calculations. Int J Hydrogen Energy 2023;48(63):24401–11. https://doi.org/10.1016/j.ijhydene.2023.03.139.
[61] Ullah MA, Riaz KN, Rizwan M. Computational evaluation of $KMgO_{3-x}H_x$ as an efficient hydrogen storage material. J Energy Storage 2023;70:108030. https://doi.org/10.1016/j.est.2023.108030.
[62] Fatima S, Rizwan M, Ullah HMN, Ali SS, Naeem H, Usman Z. Efficient hydrogen storage in $KCaF_3$ using GGA and HSE approach. Int J Hydrogen Energy 2023;48(9):3566–82. https://doi.org/10.1016/j.ijhydene.2022.10.187.
[63] Yamçıçıer Ç, Kürkçü C. Ab initio study of the structural, mechanical, optoelectronic and thermo-physical properties of $XGaH_5$ (X= Ba, Ca, and Mg) compounds for hydrogen storage applications. Int J Hydrogen Energy 2024;81:391–404. https://doi.org/10.1016/j.ijhydene.2024.07.276.
[64] Yamçıçıer Ç, Kürkçü C. Investigation of structural, electronic, elastic, vibrational, thermodynamic, and optical properties of Mg_2NiH_4 and Mg_2RuH_4 compounds used in hydrogen storage. J Energy Storage 2024;84:110883. https://doi.org/10.1016/j.est.2024.110883.
[65] Kurban M, Kürkçü C, Yamçıçıer Ç, Göktaş F. A study of structural phase transitions and optoelectronic properties of perovskite-type hydride $MgFeH_3$: ab initio calculations. J Phys Condens Matter 2019;31(30):305401. https://doi.org/10.1088/1361-648X/ab1c9e.
[66] Born M. On the stability of crystal lattices. I. Math Proc Camb Phil Soc 1940;36(2):160–72. https://doi.org/10.1017/S0305004100017138.
[67] Surucu G, Candan A, Gencer A, Isik M. First-principle investigation for the hydrogen storage properties of $NaXH_3$ (X=Mn, Fe, Co) perovskite type hydrides. Int J Hydrogen Energy 2019;44(57):30218–25. https://doi.org/10.1016/j.ijhydene.2019.09.201.
[68] Gencer A, Surucu G. Investigation of structural, electronic and lattice dynamical properties of $XNiH_3$ (X = Li, Na and K) perovskite type hydrides and their hydrogen storage applications. Int J Hydrogen Energy 2019;44(29):15173–82. https://doi.org/10.1016/j.ijhydene.2019.04.097.
[69] Surucu G, Gencer A, Candan A, Gullu HH, Isik M. $CaXH_3$ (X= Mn, Fe, Co) perovskite-type hydrides for hydrogen storage applications. Int J Energy Res 2020;44(3):2345–54. https://doi.org/10.1002/er.5062.
[70] Voigt W. Lehrbuch der Kristallphysik (Textbook of crystal physics). Leipzig und Berlin: BG Teubner; 1928.
[71] Reuß A. Berechnung der fließgrenze von mischkristallen auf grund der plastizitätsbedingung für einkristalle. ZAMM-J App Math Mech Zeitschrift für Angewandte Mathematik und Mechanik 1929;9(1):49–58. https://doi.org/10.1002/zamm.19290090104.
[72] Hill R. The elastic behaviour of a crystalline aggregate. Proc Phys Soc 1952;65(5):349. https://doi.org/10.1088/0370-1298/65/5/307.

[73] Dar SA, Srivastava V, Sakalle UK. Structural, elastic, mechanical, electronic, magnetic, thermoelectric and thermodynamic investigation of half metallic double perovskite oxide Sr_2MnTaO_6. J Magn Magn Mater 2019;484:298–306. https://doi.org/10.1016/j.jmmm.2019.04.048.

[74] Noor NA, Mahmood Q, Rashid M, Haq BU, Laref A. The pressure-induced mechanical and optoelectronic behavior of cubic perovskite $PbSnO_3$ via ab-initio investigations. Ceram Int 2018;44(12):13750–6. https://doi.org/10.1016/j.ceramint.2018.04.217.

[75] Ghani MU, Sagir M, Tahir MB, Ullah S, Assiri MA. An extensive study of structural, electronic, elastic, mechanical and optical properties of $XCdH_3$ (X=K, Rb) for hydrogen storage applications: first-principles approach. Int J Hydrogen Energy 2024;55:1265–72. https://doi.org/10.1016/j.ijhydene.2023.11.199.

[76] Zhang J, Chen Y, Chen S, Hou J, Song R, Shi ZF. First-principles study of mechanical, electronic structure, and optical properties for cubic fluoroperovskite $XMgF_3$ (X=Al, Ga, In, Tl) under high pressure. Mater Sci Semicond Process 2024;174:108158. https://doi.org/10.1016/j.mssp.2024.108158.

[77] Ranganathan SI, Ostoja-Starzewski M. Universal elastic anisotropy index. Phys Rev Lett 2008;101(5):055504. https://doi.org/10.1103/PhysRevLett.101.055504.

[78] Zener C. Elasticity and anelasticity of metals. University of Chicago Press; 1965.

[79] Vahldiek FW, Mersol SA. Anisotropy in single crystal refractory compounds: vols, vols. 1 & 2. Plenum Press; 1968.

[80] Xu N, Song R, Zhang J, Chen Y, Chen S, Li S, et al. First-principles study on hydrogen storage properties of the new hydride perovskite $XAlH_3$ (X=Na, K). Int J Hydrogen Energy 2024;60:434–40. https://doi.org/10.1016/j.ijhydene.2024.02.148.